Journal of *Marine Science and Engineering*

MDPI

Article

Fault-Tolerant Multiport Active Bridge Converter for Resilient Energy Storage Integration in Zonal Shipboard DC System

Jianjun Ma [1,*], Yijia Chen [2], Xianger Shen [2] and Yixiong Qiu [3]

[1] College of Smart Energy, Shanghai Jiao Tong University, Shanghai 200240, China
[2] Key Laboratory of Control of Power Transmission and Conversion, Ministry of Education, Shanghai Jiao Tong University, Shanghai 200240, China; chenyijiasgccjs@163.com (Y.C.); sxe123@sjtu.edu.cn (X.S.)
[3] School of Electrical Engineering, Shanghai University of Electric Power, Shanghai 200090, China; yixqiu2025@163.com
* Correspondence: j.j.ma@sjtu.edu.cn

Abstract: In this paper, the concept of a fault-tolerant multiport converter is proposed for a shipboard zonal DC system. The traditional zonal shipboard system offers a resilient power supply capability at the expense of increased cost and size. To solve this problem, the fault-tolerant multiport active bridge converter is proposed for shared energy storage between DC buses. When a short-circuit fault occurs on one bus, the energy storage can maintain uninterrupted power supply to the remaining healthy bus. With consideration of both normal operation and a fault-tolerant mode, the power transfer capability and ZVS region are analyzed. The proposed converter is compared with a traditional two-converter zonal system and multiport converter in terms of cost, volume, and efficiency. The performance of the proposed FT-MAB converter is tested through experimental verifications with the aim of validating the resilience of the power supply. The proposed FT-MAB converter achieves fault tolerance through topological reconfiguration, isolating the faulty port after the occurrence of a short-circuit fault and providing uninterrupted power supply to the healthy bus.

Keywords: shipboard zonal DC system; fault-tolerant operation; multiport converter; DC-DC converter; topology reconfiguration

check for updates

Academic Editor: Eva Loukogeorgaki

Received: 19 February 2025
Revised: 14 March 2025
Accepted: 20 March 2025
Published: 25 March 2025

Citation: Ma, J.; Chen, Y.; Shen, X.; Qiu, Y. Fault-Tolerant Multiport Active Bridge Converter for Resilient Energy Storage Integration in Zonal Shipboard DC System. *J. Mar. Sci. Eng.* **2025**, *13*, 654. https://doi.org/10.3390/jmse13040654

Copyright: © 2025 by the authors. Licensee MDPI, Basel, Switzerland. This article is an open access article distributed under the terms and conditions of the Creative Commons Attribution (CC BY) license (https://creativecommons.org/licenses/by/4.0/).

1. Introduction

The transition to DC shipboard power systems (SPSs) has become increasingly important due to advancements in power electronics which facilitate more efficient integration of energy storage systems (ESSs) and electric motor loads [1–4]. Unlike AC systems, DC allows for easier connection of distributed energy sources, contributing to a more compact shipboard architecture. It enhances system performance by enabling high-energy-density storage to balance power demands and provide backup during faults [5–7]. High-power-density storage, such as ultracapacitors, also serves to handle transient power imbalances. Moreover, DC systems also promote fuel efficiency by optimizing the operation of prime movers. With simple control, high efficiency, and better fault reconfigurability, DC microgrids are becoming the preferred choice over AC systems for modern vessels, ensuring reliable power supply for critical missions [4–7].

According to IEEE Std. 1709-2010 [1], the architecture of shipboard DC systems includes radial, ring type, zonal type, etc. Radial distribution is a simple and cost-effective architecture that is easy to redesign from a traditional AC system. However, it lacks flexibility when faults occur. In contrast, ring-type distribution offers better reliability and

survivability [4]. It connects the buses in a loop, allowing the system to isolate faults without disrupting the entire network. However, since each load center is connected to only one bus, the critical loads are still prone to bus faults. In contrast, the zonal architecture offers the highest reliability, survivability, and reconfigurability [8–10]. As shown in Figure 1, the service loads on the ship are arranged into various zones stretching from the bow to the stern, with the DC buses installed longitudinally along the vessel. Each side of the DC buses connects with two separate bidirectional DC-DC converters, allowing for flexible reconfiguration during normal operation and fault conditions. However, the cost and size of the zonal DC system will be huge, due to the high number of DC-DC converters [9,10].

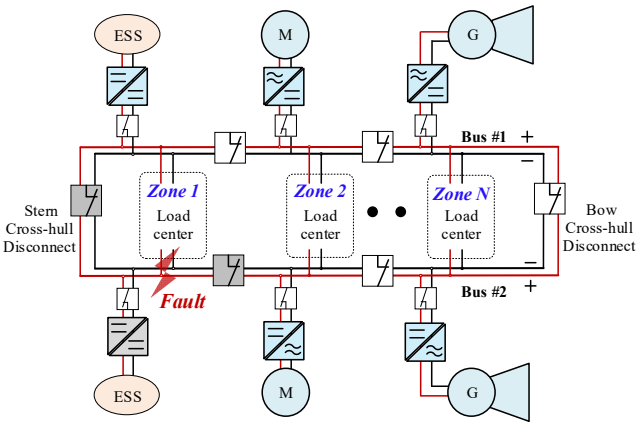

Figure 1. Configuration of the zonal shipboard DC distribution system.

One classical bidirectional DC-DC converter is the dual active bridge (DAB) converter shown in Figure 2a. * represent the dotted terminals of the transformer. It features high power density and wide voltage range zero-voltage switching (ZVS) operation capability [11]. To gain additional benefits, such as a reduced size and cost savings, the dual active half-bridge (DAHB) converter in Figure 2b can be adopted [12]. Moreover, a CLLC resonant converter can also be adopted for both ZVS and ZCS operations [13]. However, the voltage regulation range would be narrow and voltage/current stress will also increase.

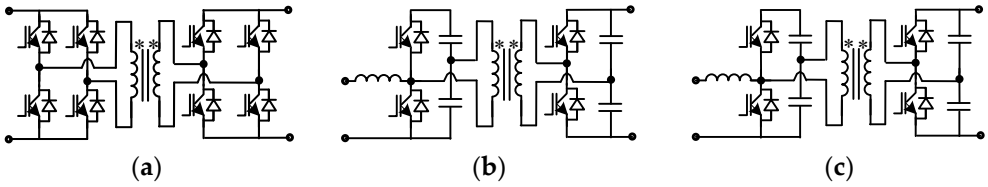

Figure 2. Classical single-input single-output DC-DC converters. (**a**) Full-bridge DAB, (**b**) half-bridge DAB, and (**c**) CLLC resonant converter.

Considering the presence of multiple DC-DC converters in DC systems, one approach to reduce a system's size and cost is to implement an integrated multiport design. Multiport converters have previously been investigated in applications such as aircraft, satellites, and electric vehicles [14–17], where compactness and efficiency are paramount. For zonal shipboard power systems, the potential multiport integration offers several advantages. On one hand, it reduces the total number of components and power conversion stages. Moreover, it allows for shared energy storage capacity. A comparison of the system's structure is illustrated in Figure 3a,b.

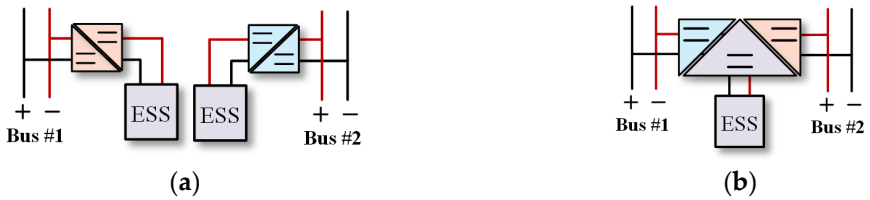

Figure 3. Integration of ESS in shipboard DC systems: (**a**) two-converter and two-ESS system and (**b**) proposed fault-tolerant multiport converter and shared ESS.

Depending on the circuit topology, existing multiport converters can be classified into non-isolated [17–19], partially isolated [20], and fully isolated types [21–23]. For example, a non-isolated multiport converter has a simple topology and low component number. However, the converter efficiency and voltage range will be low. Based on the partially isolated converters in Figure 4b and fully isolated triple active bridge (TAB) converter in Figure 4c, both zero-voltage switching and a wide voltage regulation ratio can be achieved [22]. Most existing multiport converters focus on efficiency elevation and cost reduction [17,18]. However, the integrated design often comes at the expense of reliability.

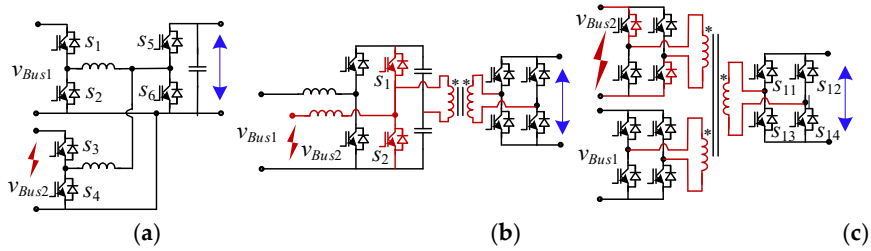

Figure 4. Fault performance of conventional multiport converters: (**a**) non-isolated converter [18], (**b**) partially isolated converter [20], and (**c**) fully isolated converter [22].

The FT-MAB converter aims to tackle frequent bus short-circuit faults in shipboard DC systems using fault-tolerance. Short-circuit faults, caused by insulation degradation or aging in harsh environments, can lead to high-current surges and system collapse. Open-circuit faults, causing gradual power loss, are less urgent as the system can switch to alternate power sources. For instance, in Figure 4a, if the short-circuit fault occurs on $v_{bus}2$, it will result in the shutdown of the shared switches S_5 and S_6. Otherwise, the high fault current will flow through the antiparallel diode of S_3. Similarly, when a fault occurs on $v_{bus}2$ of Figure 4b, the shared power switches S_5 and S_6 will be blocked and the whole converter drops out. For the fully isolated TAB in Figure 4c, if a short-circuit fault occurs on $v_{Bus}2$, the primary side switches S_{11}~S_{14} need to be blocked to limit the fault current. As a result, the healthy bus $v_{Bus}1$ will also drop out.

As shown in Table 1, to achieve both an integrated design and enhanced system reliability, the fault-tolerant multiport converter is first proposed for shipboard DC systems. In the existing studies on the control and modulation of DAB (Dual Active Bridge) converters [24,25], research has focused on optimizing control algorithms for traditional DAB or ISOP-DAB systems. However, the FT-MAB converter proposes a multi-port reconfigurable topology that achieves fault tolerance through hardware-level design, breaking through the limitations of current research, which is predominantly driven by control optimization.

According to IEEE Std. 1826-2020 [26], compared to traditional systems with independent energy storage units, the proposed FT-MAB converter ensures that at least one healthy energy path remains available during any short-circuit fault, thereby providing a robust solution to fault tolerance in shipboard DC systems.

Table 1. Contributions of this paper.

Integrated Multiport Design	Fault-Tolerant Operation	References
✓	✗	[18,20,22]
✗	✓	[8,21,27]
✓	✓	Proposed work

The rest of this paper is organized as follows: in Section 2, the modulation of the proposed FT-MAB converter is analyzed in both normal and fault-tolerant modes. In Section 3, the power transfer capability and soft switching performance of the converter are evaluated in the two working modes. In Section 4, the proposed FT-MAB converter is quantitively compared with a traditional two-converter zonal system and multiport full-bridge converter, in terms of cost, volume, and power loss. The proposed converter is tested under normal operation and short-circuit conditions, verifying the proposed topology and modulation methods.

2. Operation Principles

The topology of the fault-tolerant multiport active bridge (FT-MAB) converter is shown in Figure 5. The converter consists of two half-bridges (HB), including switches S_{11}, S_{12}, S_{21}, and S_{22}, each connected to one of the two DC buses, Bus #1 or Bus #2, in the zonal DC power system. The two HBs are connected with the three-arm full-bridge (TAFB) through two transformers, respectively, including switches S_{31}, S_{32}, S_{41}, S_{42}, S_{51}, and S_{52}. The energy storage system is connected to the DC port of the TAFB. According to the operation condition, the working modes of the FT-MAB can be classified as the normal operation mode and fault-tolerant mode.

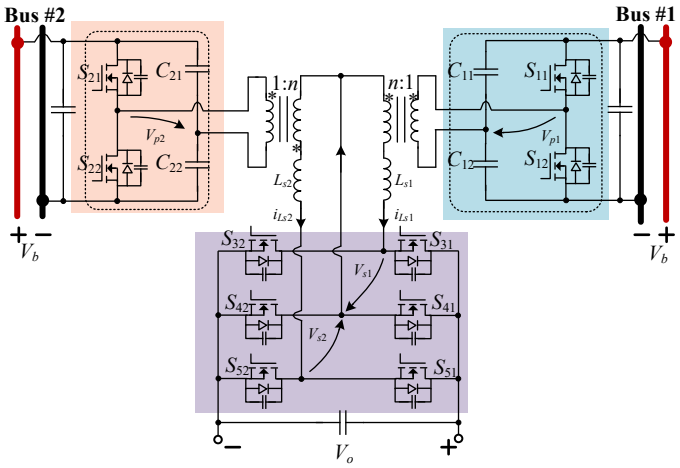

Figure 5. Topology of the fault-tolerant multiport active bridge converter.

2.1. Normal Operation

During normal operation, bidirectional power can be transferred between energy storage and the two DC buses (i.e., Bus #1 and Bus #2). Moreover, mutual power support between Bus #1 and Bus #2 can also be achieved through the multiport converter, depending on the phase shift duty ratios d_1 and d_2, as analyzed in the following.

2.1.1. Same Power Direction of DC Buses

Depending on the phase shift duty ratios d_1 and d_2, the energy storage can simultaneously supply power to two DC buses or receive power from them. Without loss of

generality, the case when $d_1 > 0$ and $d_2 > 0$ is considered. The key waveforms for this scenario are illustrated in Figure 6a, where the storage is charged from both buses. The switching states for this case are as follows:

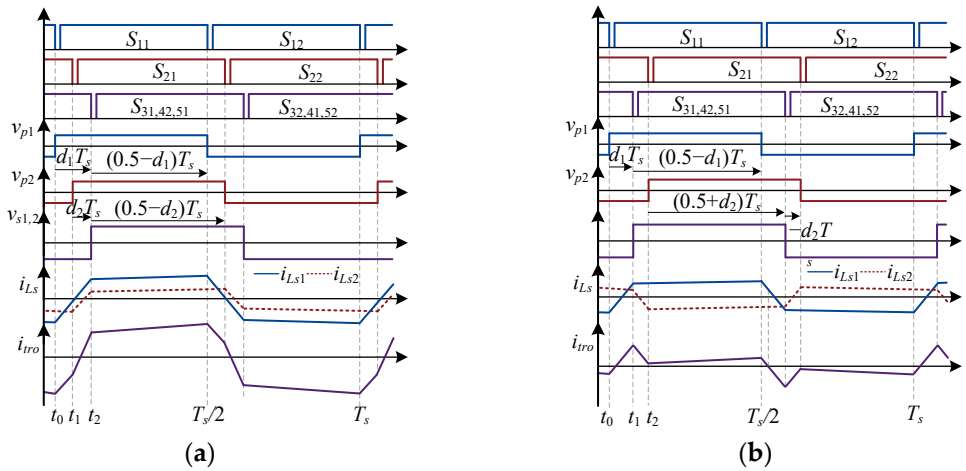

Figure 6. Key waveforms of the FT-MAB in the normal dual-bus mode: (**a**) $d_1 > 0$ and $d_2 > 0$ and (**b**) $d_1 > 0$, $d_2 < 0$.

Switching state 1 [t_0, t_1]: At t_0, S_{12} is turned off and the inductor current i_{Ls1} is of negative value. Within the switching dead time, the parasitic capacitor of S_{12} is charged to bus voltage V_b and the parasitic capacitor of S_{11} discharges to 0. As a result, S_{11} can be turned on with zero voltage switching (ZVS). During this period, the inductor currents i_{Ls1} and i_{Ls2} are given as shown in (1).

$$\begin{cases} i_{Ls1}(t) = i_{Ls1}(t_0) + (t - t_0)(nV_b/2 + V_o)/L_{s1} \\ i_{Ls2}(t) = i_{Ls2}(t_0) + (t - t_0)(-nV_b/2 + V_o)/L_{s2} \end{cases} \tag{1}$$

where V_b is the DC bus voltage and V_o is the ESS voltage. n is the transformer turns ratio and L_{s1} and L_{s2} are the equivalent series inductance. At the secondary side of the converter, the current flowing through the shared switches S_{41} and S_{42} is the sum of the two inductor currents (Figure 5), as given by i_{tro} in (2).

$$i_{tro}(t) = i_{Ls1}(t) + i_{Ls2}(t) \tag{2}$$

Switching state 2 [t_1, t_2]: At t_1, S_{22} is turned off and the inductor current i_{Ls2} is negative. Within the switching dead time, the parasitic capacitor of S_{22} is charged to bus voltage V_b and the parasitic capacitor of S_{21} discharges to 0. As a result, S_{11} can be turned on with zero voltage switching (ZVS). During this period, the inductor currents i_{Ls1} and i_{Ls2} are given as shown in (3).

$$\begin{cases} i_{Ls1}(t) = i_{Ls1}(t_1) + (t - t_1)(nV_b/2 + V_o)/L_{s1} \\ i_{Ls2}(t) = i_{Ls2}(t_1) + (t - t_1)(nV_b/2 + V_o)/L_{s2} \end{cases} \tag{3}$$

Switching state 3 [t_2, $T_s/2$]: At t_2, S_{32}, S_{41}, and S_{52} are turned off. According to the direction of i_{Ls1}, i_{Ls2}, and i_{tro}, within the switching dead time, the parasitic capacitors of S_{32}, S_{41}, and S_{52} are charged. On the other hand, the parasitic capacitors of the complementary

switches S_{31}, S_{42}, and S_{51} are discharged. As a result, ZVS-on of S_{31}, S_{41}, and S_{51} can be guaranteed. In this period, the inductor currents i_{Ls1} and i_{Ls2} are given as shown in (4).

$$\begin{cases} i_{Ls1}(t) = i_{Ls1}(t_2) + (t - t_2)(nV_b/2 - V_o)/L_{s1} \\ i_{Ls2}(t) = i_{Ls2}(t_2) + (t - t_2)(nV_b/2 - V_o)/L_{s2} \end{cases} \tag{4}$$

2.1.2. Mutual Power Support Between DC Buses

When the phase-shifted duty ratios d_1 and d_2 have different signs, the system can achieve mutual power support between the two DC buses. Without loss of generality, we consider here the case $d_1 > d_2 > 0$. The corresponding modulation waveforms are shown in Figure 6b. In this scenario, the power is transferred from Bus #1 to Bus #2 as well as the energy storage.

Similar to the switching state analysis in the above Figure 6a, the switching states in Figure 6b can be divided into three stages, due to the circuit symmetry. The inductor currents i_{Ls1} and i_{Ls2} during each switching state are given as follows.

Switching state 1 [t_0, t_1]:

$$\begin{cases} i_{Ls1}(t) = i_{Ls1}(t_0) + (t - t_0)(nV_b/2 + V_o)/L_{s1} \\ i_{Ls2}(t) = i_{Ls2}(t_0) + (t - t_0)(-nV_b/2 + V_o)/L_{s2} \end{cases} \tag{5}$$

Switching state 2 [t_1, t_2]:

$$\begin{cases} i_{Ls1}(t) = i_{Ls1}(t_1) + (t - t_1)(nV_b/2 - V_o)/L_{s1} \\ i_{Ls2}(t) = i_{Ls2}(t_1) + (t - t_1)(-nV_b/2 - V_o)/L_{s2} \end{cases} \tag{6}$$

Switching state 3 [t_2, $T_s/2$]:

$$\begin{cases} i_{Ls1}(t) = i_{Ls1}(t_2) + (t - t_2)(nV_b/2 - V_o)/L_{s1} \\ i_{Ls2}(t) = i_{Ls2}(t_2) + (t - t_2)(nV_b/2 - V_o)/L_{s2} \end{cases} \tag{7}$$

2.2. Fault-Tolerant Operation

When a short-circuit fault occurs at one of the DC buses, the FT-MAB serves to isolate the fault and supplies power to the healthy bus. Without loss of generality, we assume here that the fault occurs at Bus #1.

After detected the fault, S_{11}, S_{12}, S_{31}, and S_{32} are blocked. The remaining switches (S_{21}~S_{22} and S_{41}~S_{52}) keep in operation. The equivalent circuit in the fault-tolerant mode is shown in Figure 7. It operates similarly to the single-input single-output dual active bridge converter.

The modulation waveforms in the fault-tolerant mode are depicted in Figure 8. Similarly to DAB, it consists of two switching states. The inductor current i_{Ls2} in each state is given in the following.

Switching state 1 [t_0, t_1]:

$$\begin{cases} i_{Ls1}(t) = 0 \\ i_{Ls2}(t) = i_{Ls2}(t_0) + (t - t_0)(nV_b/2 + V_o)/L_{s2} \end{cases} \tag{8}$$

Switching state 2 [t_1, $T_s/2$]:

$$\begin{cases} i_{Ls1}(t) = 0 \\ i_{Ls2}(t) = i_{Ls2}(t_1) + (t - t_1)(nV_b/2 - V_o)/L_{s2} \end{cases} \tag{9}$$

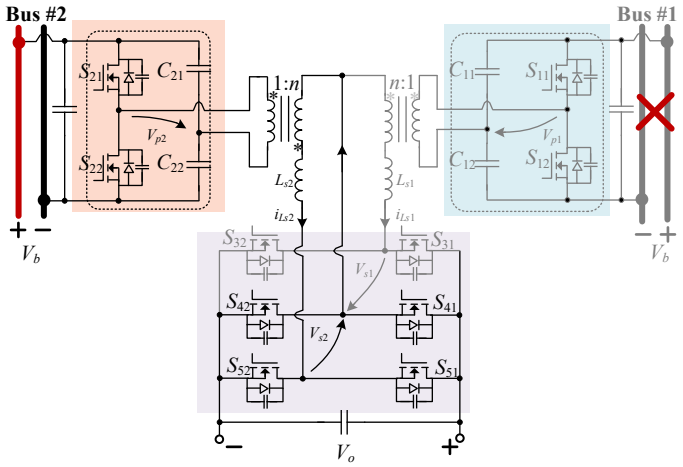

Figure 7. Equivalent circuit of the FT-MAB in the fault-tolerant mode.

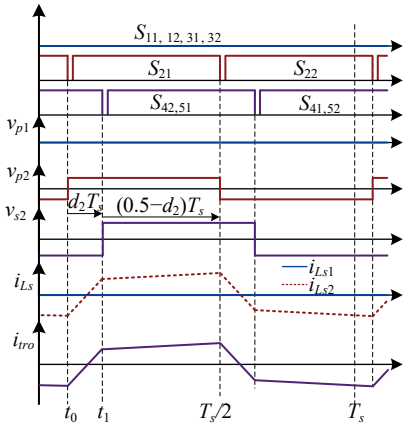

Figure 8. Key waveforms of the FT-MAB in the fault-tolerant mode.

3. Performance Analysis

With consideration of both normal operation and fault-tolerant conditions, the performance of the FT-MAB converter is analyzed in this section, including the power transfer capability and soft-switching performance.

3.1. Power Transfer Capability

Based on Figure 6a, when $d_1 > 0$ and $d_2 > 0$, the power transfer from Bus #1 (Bus #2) to the energy storage P_1 (P_2) is given as shown in (10).

$$\begin{cases} P_1 = \frac{2}{T_s}\left(\int_{t_0}^{t_1}(nV_b/2 - V_o)i_{Ls1}dt + \int_{t_1}^{T_s/2}(nV_b/2 + V_o)i_{Ls1}dt\right) \\ P_2 = \frac{2}{T_s}\left(\int_{t_0}^{t_2}(nV_b/2 - V_o)i_{Ls2}dt + \int_{t_2}^{T_s/2}(nV_b/2 + V_o)i_{Ls2}dt\right) \end{cases} \tag{10}$$

Due to the symmetry of the circuit, here we assume $L_{s1} = L_{s2} = L_s$. By combing (1)–(4) with (10), the converter output powers P_1 and P_2 are given as shown in (11).

$$\begin{cases} P_1 = \frac{Mn^2V_b^2d_1(1-2d_1)}{2fL_s}d_1 > 0 \\ P_2 = \frac{Mn^2V_b^2d_2(1-2d_2)}{2fL_s}d_2 > 0 \end{cases} \tag{11}$$

where f is the switching frequency, $f = 1/T_s$. M is the voltage conversion ratio defined by (12).

$$M = \frac{V_o}{nV_b} \tag{12}$$

Based on (11) and (12), the total output power P_o is given by

$$P_o = P_1 + P_2 = \frac{Mn^2 {V_b}^2 [d_1(1-2d_1) + d_2(1-2d_2)]}{2fL_s} \tag{13}$$

Based on (11)–(13), the maximum power transfer between the DC buses and the energy storage can be obtained at $d_1 = d_2 = 0.25$. The corresponding maximum bus powers P_{1max} and P_{2max} and total power P_{max} are given by (14).

$$P_{1max} = P_{2max} = \frac{Mn^2 {V_b}^2}{16fL_s}, P_{omax} = \frac{Mn^2 {V_b}^2}{8fL_s} \tag{14}$$

Similarly, based on (5)–(7), when $d_1 > 0$ and $d_2 < 0$, P_1, P_2, and P_o can be derived as shown in (15). Since $d_2 < 0$, $P_2 < 0$ always holds in (11), which indicates Bus #2 receives power. The maximum power (P_2) transfer from the energy storage to Bus #2 can be obtained when $d_2 = -0.25$. Moreover, the maximum power from Bus #1 is obtained at $d_1 = 0.25$. The maximum values of P_1 and P_2 are the same as given in (14).

Furthermore, based on (11) and (15), the input power of the two DC buses can be independently regulated by the two control variables d_1 and d_2. It can be observed that P_1 is irrelevant to d_2 and P_2 is irrelevant to d_1, which would facilitate decoupled power regulation.

$$\begin{cases} P_1 = \frac{Mn^2 {V_b}^2 d_1(1-2d_1)}{2fL_s} d_1 > 0 \\ P_2 = \frac{Mn^2 {V_b}^2 d_2(1+2d_2)}{2fL_s} d_2 < 0 \\ P_o = \frac{Mn^2 {V_b}^2 [d_1(1-2d_1)+d_2(1+2d_2)]}{2fL_s} \end{cases} \tag{15}$$

In the fault-tolerant mode, the converter output power can be developed based on (8) and (9), as shown in (16). Similar to DAB, during the fault-tolerant mode, the output power can be independently regulated with the phase shift ratio d_2.

$$P_o = P_2 = \frac{Mn^2 {V_b}^2 d_2(1-2d_2)}{2fL_s} \tag{16}$$

Comparing (16) with (15), the maximum output power P_o in the normal operation mode is exactly twice the maximum output power in the fault-tolerant mode. On the other hand, the power rating between the healthy bus and the energy storage remains unchanged after fault-tolerant reconfiguration.

3.2. Soft Switching Performance

Based on the switching state analysis in Section 2.1, the ZVS conditions for each switch are listed in Table 2.

Table 2. ZVS Constraints in normal mode.

Switches	S_{11}, S_{12}	S_{21}, S_{22}	S_{31}, S_{32}	S_{41}, S_{42}	S_{51}, S_{52}
ZVS Criterion $d_1 > 0$ and $d_2 > 0$ (in Figure 6a)	$i_{Ls1}(t_0) < 0$	$i_{Ls2}(t_1) < 0$	$i_{Ls1}(t_2) > 0$	$i_{tro}(t_2) > 0$	$i_{Ls2}(t_2) > 0$
ZVS Criterion $d_1 > 0$ and $d_2 < 0$ (in Figure 6b)	$i_{Ls1}(t_0) < 0$	$i_{Ls2}(t_2) < 0$	$i_{Ls1}(t_1) > 0$	$i_{tro}(t_1) > 0$	$i_{Ls2}(t_1) > 0$

Based on (1), (3), and (4), when $d_1 > 0$ and $d_2 > 0$, the inductor currents i_{Ls1}, i_{Ls2}, and i_{tro} at the instants when the corresponding switches are turned on are derived as shown in (17). By combing (17) and Table 1, the ZVS operation region can be developed.

Similarly, when $d_1 > 0$ and $d_2 < 0$, the expressions of i_{Ls1}, i_{Ls2}, and i_{tro} at the instants when the correlated switches are turned on are derived as shown in (18).

$$\begin{matrix} d_1 > 0 \\ d_2 > 0 \end{matrix} \begin{cases} i_{Ls1}(t_0) = -\frac{nV_b(8d_1M-2M+1)}{8fL_s} \\ i_{Ls1}(t_2) = \frac{nV_b(4d_1-1+2M)}{8fL_s} \\ i_{Ls2}(t_1) = -\frac{nV_b(8d_1M-2M+1)}{8fL_s} \\ i_{Ls2}(t_2) = \frac{nV_b(4d_2-1+2M)}{8fL_s} \\ i_{tro}(t_2) = i_{Ls1}(t_2) + i_{Ls2}(t_2) \\ \qquad\quad = \frac{nV_b(2d_1+2d_2-1+2M)}{4fL_s} \end{cases} \tag{17}$$

$$\begin{matrix} d_1 > 0 \\ d_2 < 0 \end{matrix} \begin{cases} i_{Ls1}(t_0) = -\frac{nV_b(8d_1M-2M+1)}{8fL_s} \\ i_{Ls1}(t_1) = \frac{nV_b(4d_1-1+2M)}{8fL_s} \\ i_{Ls2}(t_1) = \frac{nV_b(-4d_2-1+2M)}{8fL_s} \\ i_{Ls2}(t_2) = -\frac{nV_b(-8d_2M-2M+1)}{8fL_s} \\ i_{tro}(t_1) = i_{Ls1}(t_1) + i_{Ls2}(t_1) \\ \qquad\quad = \frac{nV_b(2d_1-2d_2-1+2M)}{4fL_s} \end{cases} \tag{18}$$

According to (17) and (18), the ZVS constraints of S_{11}, S_{12}, S_{31}, and S_{32} are irrelevant to d_2. Similarly, the ZVS constraints of S_{21}, S_{22}, S_{51}, and S_{52} are irrelevant to d_1. In addition, when the ZVS conditions of S_{31}, S_{32}, S_{51}, and S_{52} are met, the ZVS operation of S_{41} and S_{42} is automatically achieved. The physical explanation is that the current flow through S_{41} and S_{42} is the sum of i_{Ls1} and i_{Ls2}.

By combing (17) and (18) with Table 2, the soft-switching condition of the duty ratio with respect to the voltage conversion ratio M is given as shown in (19).

$$|d| > max\{\frac{1-2M}{4}, \frac{2M-1}{8M}\} \tag{19}$$

By combing (19) with (13) and (15), the ZVS operation region of output power with the voltage conversion ratio M is shown in Figure 9.

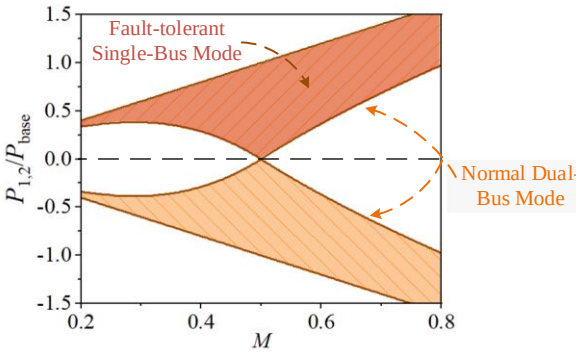

Figure 9. ZVS operation region of the FT-MAB converter.

In the fault-tolerant mode, the soft-switching conditions are given as shown in Table 3. By comparing Table 3 with Table 2, it is also found that the ZVS-on constraints given by (19) also applies to the fault-tolerant mode. As a result, the fault-tolerant operation region overlaps with the normal operation.

Table 3. ZVS constraints in fault-tolerant mode.

Switches	S_{21}, S_{22}	S_{41}, S_{42}	S_{51}, S_{52}
ZVS Criterion (in Figure 8)	$i_{Ls2}(t_1) < 0$	$i_{tro}(t_2) > 0$	$i_{Ls2}(t_2) > 0$

3.3. Control Design

The control aims of the FT-MAB include input power P_1 and P_2. The control diagram is shown in Figure 10.

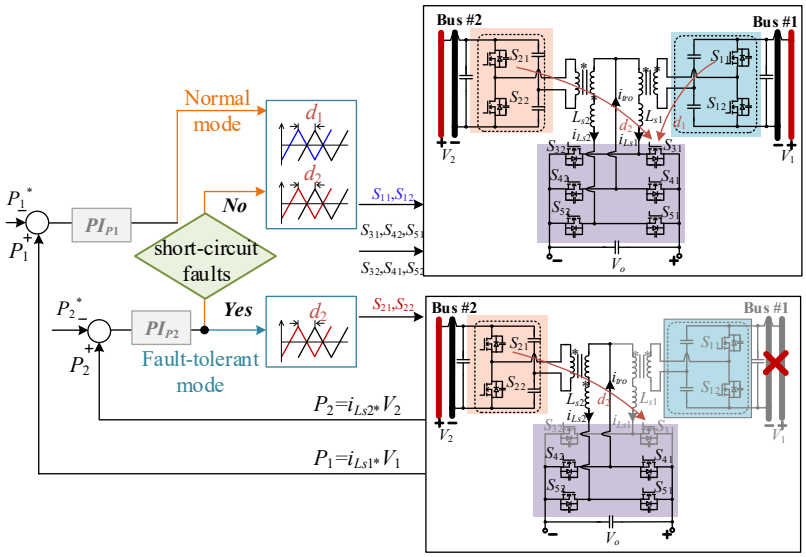

Figure 10. Control of FT-MAB with power regulation.

With consideration of the bidirectional power transfer need, the forward/backward working mode as well as the total output power can be regulated with the phase-shift duty ratios d_1 and d_2. When the phase-shifted duty ratios d_1 and d_2 have different signs, the system can achieve mutual power support between the two DC buses. When the FT-MAB converter operates in the normal mode, the power is transferred from Bus #1 and Bus #2 to the energy storage. The specific values of d_1 and d_2 are determined by the controller PI_{P1} and PI_{P2}. When the FT-MAB converter operates in the fault-tolerant mode, Bus #1 is short-circuited and $P_1 = 0$. The power is transferred from Bus #2 to the energy storage. The specific value of d_2 is determined by the controller PI_{P2}.

4. Circuit Comparison

In this section, the performance of the proposed FT-MAB is evaluated in comparison with a traditional dual-module system (Figure 3a). The classical DAB converter is adopted in the two-module system as an input-independent output-parallel DAB (IIOP-DAB). The detailed circuit is shown in Figure 11a. Moreover, if the full bridge is adopted at the bus side, the full-bridge dual-transformer asymmetrical triple-port active bridge (DT-ATAB) is illustrated in Figure 11b.

The conventional converters in Figure 10 are compared with the proposed FT-MAB under the same scenario, with the system parameters listed in Table 4.

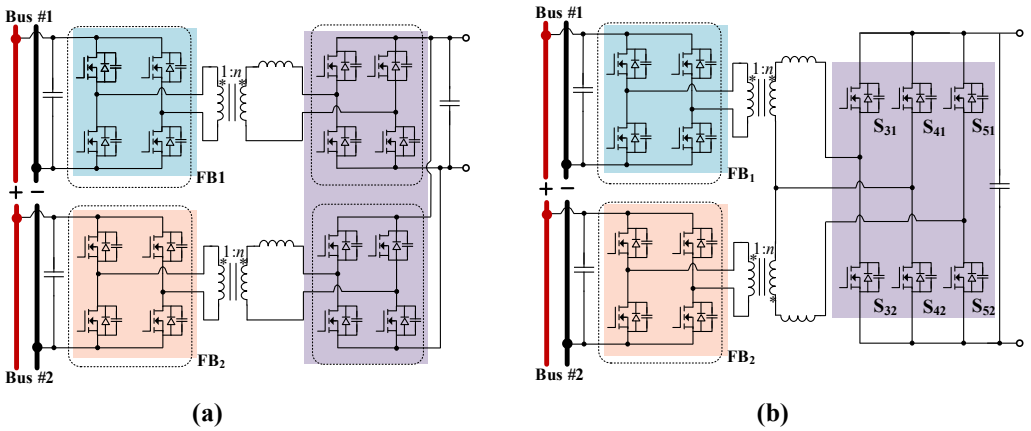

Figure 11. Representative converters for topology comparison: (**a**) IIOP-DAB and (**b**) DT-ATAB.

Table 4. Mode scenario for the topology comparison.

Parameter	Value
Bus voltage $V_{bus}1$, $V_{bus}2$	750 V, 750 V
Output power P_o	15 kW
Output voltage V_o	400 V
Switching frequency f_s	40 kHz

4.1. Cost Comparison

For a fair cost comparison, all semiconductor switches are selected from Infineon and the drivers are selected from Microchip products. Their prices are sourced from Digi-Key Electronics [28]. Considering the voltage/current stress margin, the semiconductor switches selected for each converter are listed in Table 5.

Table 5. Component selection for case study.

Items		Proposed	IIOP-DAB	DT-ATAB
Peak current through switches/A	Input-side	27	17	17
	Output-side	60	30	60
Switches	Input-side	FF6MR 12W2M1H_B11	FF33MR12W1M1HP_B11	
	Output- side		FF33MR12W1M1HP_B11	
	Output- shared switches (S_{41}, S_{42})		/	FF6MR12W2M1H_B11
Magnetic components	Transformer core	1	0P49925UC	0.5
	turns ratio n		0.5	
	Inductor core		0077774A7	
Capacitors	Bus-side	B32373B4107J080	C44USGT6120M81K	
	Load-side	B32371A3806J030	C4DEIPQ6100A8TK	B25631B0127K800
Driver	2ASC-12A2HP			

The switches used in the input stage of all three converters are FF33MR12W1M1HP_B11. For the FT-MAB converter and DT-ATAB converter, the output-side bridge current stress is increased to twice the value and the switch module used is FF6MR12W2M1H_B11.

The transformer turns ratio is designed as 15:15 for the proposed FT-MAB. As for the DT-ATAB converter and ISOP-DAB converter, the transformer turns ratio is selected as 30:15. All three converters use 0.1 mm × 1500 litz wire, with the core material selected as 0P49928EC. The series inductors utilize 0077774A7 magnetic cores. The prices for the magnetic components can be found in [28].

Under the condition of the same power rating, the cost of transformers and inductors is related to their quantity, current stress, and winding configuration. The bus-side and load-side capacitors for these three converter systems are determined with the same voltage ripple ratio of 1%.

A comparison of the total converter cost is shown in Figure 12. Due to the reduced number of switches, the cost of switches and drivers of the proposed FT-MAB converter is significantly lower. Considering the increased number of DC-link capacitors, their impact on the total capacitance and converter cost is relatively small. As a result, the proposed FT-MAB exhibits the lowest total converter cost.

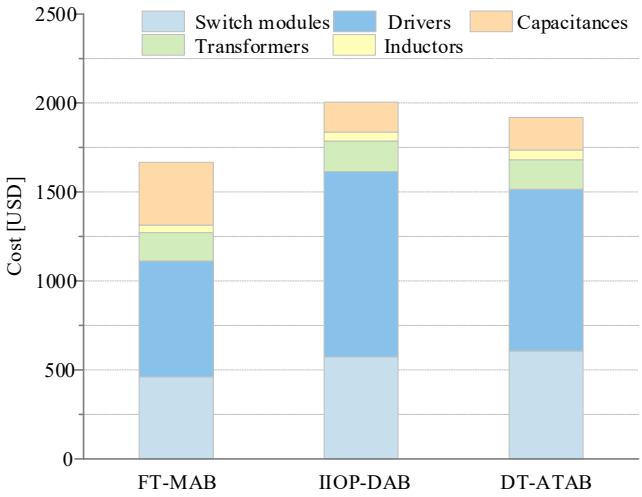

Figure 12. Cost comparison of the three topologies.

4.2. Volume Comparison

Based on the component selection listed in Table 5 and the size parameters, the corresponding volume of each converter can be calculated. As shown in Figure 13, the main influencing factors for the converter volume are the capacitors and the transformer/inductors. The size of inductance is also influenced by the voltage rating. Since the full-bridge circuit has a higher voltage stress, the inductance volume is comparatively larger than that of the half-bridge in the FT-MAB. On the other hand, the proposed FT-MAB has a higher number of capacitors and the total capacitor volume is much higher. As a result, the total sizes of all three converters are similar.

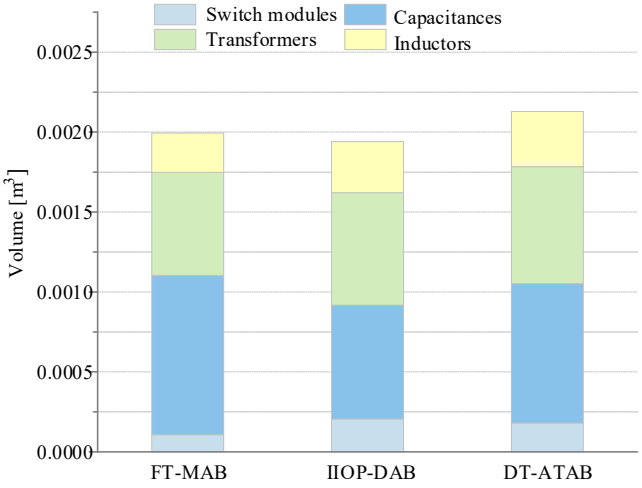

Figure 13. Volume comparison of three topologies.

4.3. Loss Comparison

The converter power loss mainly consists of switch losses, transformer losses, capacitor losses, and inductor losses.

Transformer/inductor power losses includes core losses and copper losses. The transformer core material is selected as 0P49925UC, with the assumption that the high-frequency transformer operates at a temperature of 80 °C and the maximum operating magnetic flux density is designed at 0.2 T. To mitigate the skin effect, litz wire is adopted. The winding current density of the high-frequency transformer is set to 3 A/mm^2. Based on the Steinmetz equation and transformer calculation formulas, the power losses of the high-frequency transformer are calculated. The inductor core material is selected as 0077774A7 and the total loss is determined by a calculation tool provided by the manufacturer [29].

The power loss of switches includes conduction losses and switching losses. Based on the datasheet provided by Infineon, the power losses of the switches are simulated using PLECS (4.8.4) thermal software. In comparison, the converter loss breakdown is shown in Figure 14a. Compared with IIOP-DAB and DT-ATAB, the proposed FT-MAB has the smallest power loss. Based on the PLECS simulation software, the efficiency curve of the proposed converter and traditional systems (IIOP-DAB) is plotted as shown in Figure 14b. It can be seen that the FT-MAB converter has a significant efficiency advantage. Specifically, the highest efficiency is achieved at an output power of 10 kW, which is consistent with the experimental results.

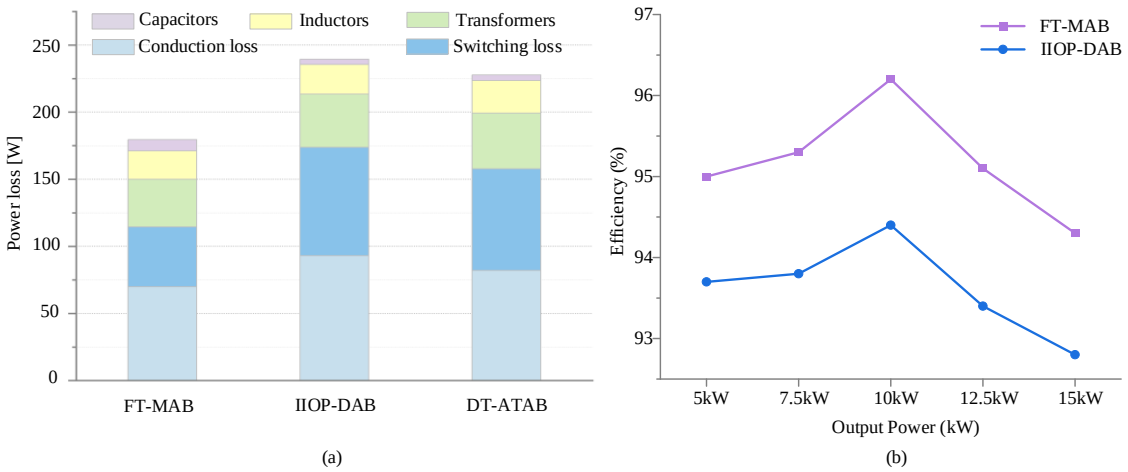

Figure 14. Efficiency comparison. (**a**) Loss comparison of the three topologies and (**b**) efficiency comparison between the proposed converter and traditional systems.

5. Experimental Verifications

The proposed FT-MAB converter and operation strategy are tested with an experimental prototype. Parameters of the prototype are listed in Table 6. The switches and diodes are implemented with IRFP260N and MBR40200PT, respectively, and the control is implemented with a TI C6657 DSP controller. The photograph of the experimental platform is shown in Figure 15. Two regenerative DC power supplies are connected to the DC side of the half bridges, serving as the power supply for the two buses, respectively. Another regenerative DC power supply is connected to the DC side of the full bridge to simulate a bidirectional load. The experimental platform verifies the feasibility and characteristics of the FT-MAB operating in both normal and fault-tolerant modes.

Table 6. Parameters of the experimental prototype.

Parameter	Value
Input voltage $V_{bus}1$, $V_{bus}2$	48 V
Output voltage V_o	110 V
Rated output power P_{or}	200 W
Switching frequency f_s	40 kHz
Series inductance L_s	65 µH
Transformer turns ratio	1:1

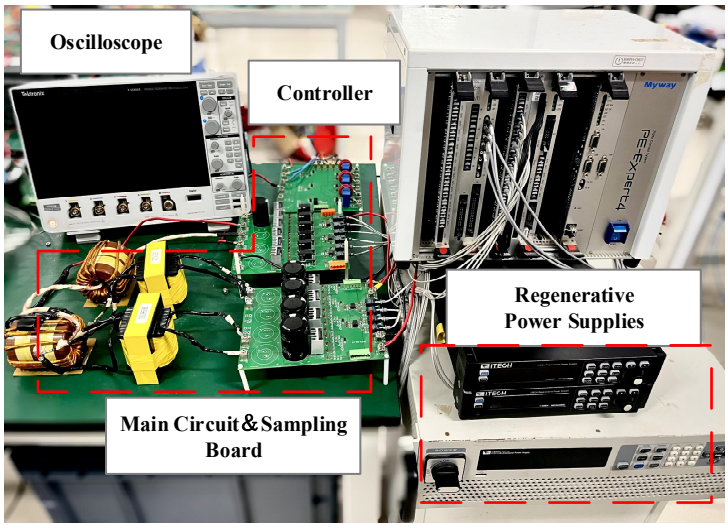

Figure 15. A photograph of the hardware setup.

5.1. Steady-State Operation and ZVS Characteristics

The steady-state waveforms of the FT-MAB converter in the normal dual-bus mode are shown in Figure 16.

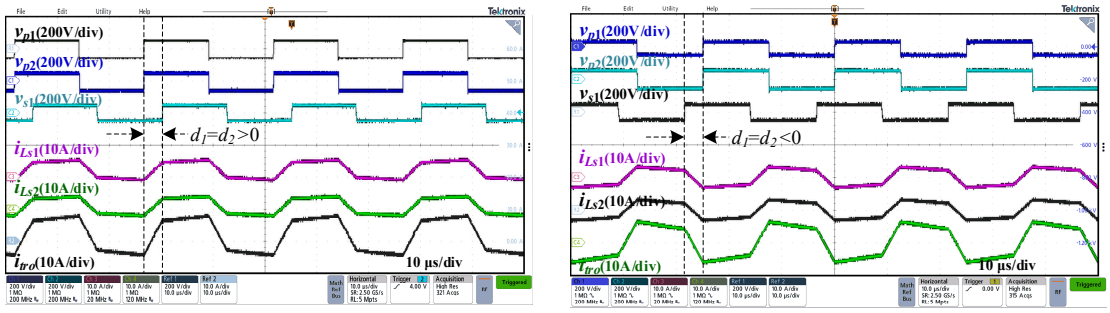

(**a**) (**b**)

Figure 16. Steady-state waveforms of the converter in dual-bus mode: (**a**) Forward power transfer, $P_1 = P_2$, and (**b**) reverse power transfer, $P_1 = P_2$.

As can be observed in Figure 16, by regulating the phase-shift duty ratios, the output voltage v_{p1}, v_{p2} leads v_{s1} in the forward mode and v_{s1} leads v_{p1}, v_{p2} in the backward power mode.

Moreover, by independently regulating the phase-shift duty ratios d_1 and d_2, the output power of the two DC buses can be controlled. The corresponding operation waveforms are illustrated in Figure 17a,b. The modulation waveforms are in accordance with the analysis in Section 2.1.

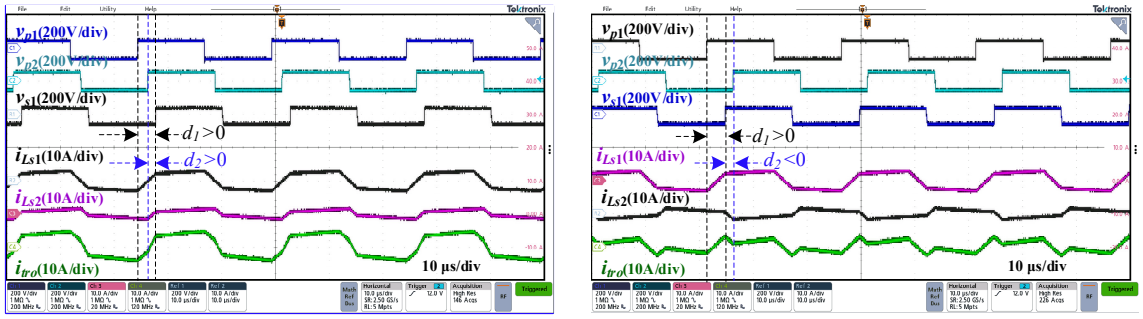

(**a**) (**b**)

Figure 17. Steady-state waveforms of the converter in normal dual-bus mode: (**a**) Forward power transfer, $P_1 \neq P_2$, and (**b**) reverse power transfer, $P_1 \neq -P_2$.

In comparison, in the fault-tolerant mode, the modulation waveforms are illustrated in Figure 16.

In Figure 18, when short-circuit fault occurs in Bus1, S_{11}, S_{12}, S_{31}, and S_{32} are blocked and v_{p1} is constantly 0. The modulation waveforms are in accordance with the modulation in Figure 8. By controlling the phase-shift ratio d_2, bidirectional power can still be regulated after a short-circuit fault. The fault-tolerant operation is in accordance with the analysis in Section 2.2.

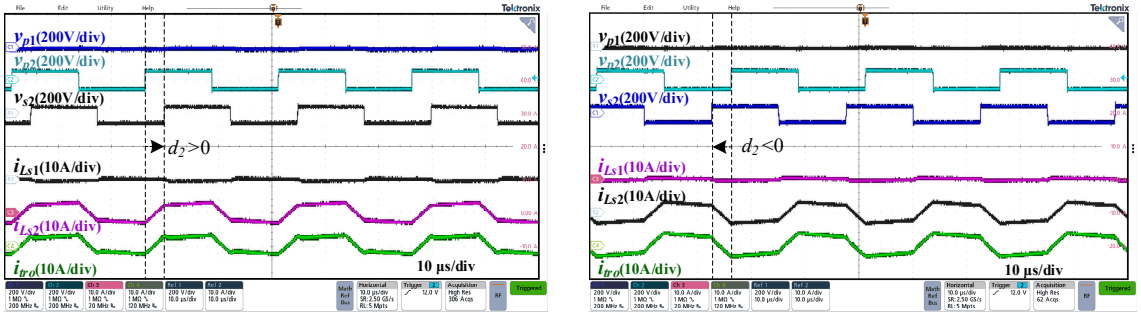

(**a**) (**b**)

Figure 18. Steady-state waveforms of the converter in fault-tolerant single-bus mode: (**a**) Forward power transfer and (**b**) reverse power transfer.

In verification of the soft-switching performance, the zoomed-out waveform at the switching instant in normal mode and fault-tolerant mode are shown in Figure 19a and 19b, respectively. Before the driving signal V_{gsS11}, V_{gsS31} reaches, the voltage across the switch V_{dsS11}, V_{dsS31} first drops to 0. As a result, the ZVS for power switches is guaranteed, in accordance with the analysis in Section 3.2.

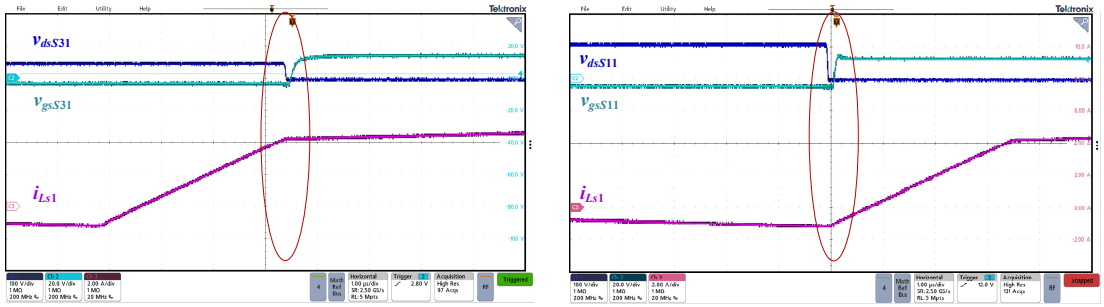

(**a**) (**b**)

Figure 19. Zoomed-out waveforms of ZVS operation. (**a**) ZVS of S_{31} in the normal dual-bus mode. (**b**) ZVS of S_{11} in the fault-tolerant single-bus mode.

5.2. Fault-Tolerant Operation

The fault-tolerant operation of the FT-MAB converter is tested in Figure 20. Before time t_1, the converter operates stably in the normal dual-bus mode. At time t_1, a short-circuit fault occurs on Bus 1 of the converter, which leads to a significant decrease in the bus voltage v_{bus1}.

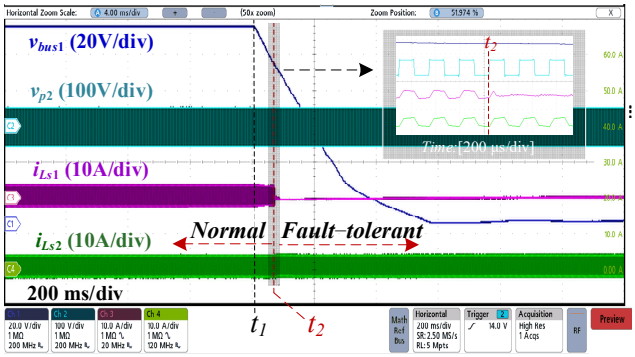

Figure 20. Transition between the normal mode and fault-tolerant mode after Bus #1 short-circuit fault.

When the bus voltage v_{bus1} drops below 70% of the normal value at time t_2, the undervoltage protection is triggered. Consequently, the switching pulses of S_{11}, S_{12}, S_{31}, and S_{32} are blocked. As a result, the primary-side current i_{Ls1} of the corresponding transformer drops to 0. Meanwhile, the driving signals of S_{21}, S_{22}, and S_{41}~S_{52} remain in operation. The fault tolerant operation is in accordance with the analysis in Section 2.2.

This paper experimentally validates the fault-tolerant capability and efficiency characteristics of the FT-MAB converter based on a low-power prototype. However, in high-power scenarios such as shipboard DC systems, several issues need to be further considered. For example, the conduction and switching losses of switching devices significantly increase at high power levels. The solution can adopt a modular multilevel converter (MMC) structure to reduce the voltage stress on the switches.

5.3. Efficiency

Precise measurements of the efficiency of the FT-MAB converter in both normal and fault-tolerant modes were conducted by collecting data. LEM LV 25-P voltage sensors and LEM LA 55-P current sensors were used to capture voltage and current signals at each port, respectively. The sampling frequency was set to ensure complete recording of high-frequency switching transients. Multi-channel signal synchronized acquisition was achieved using a National Instruments (NI) USB-9234 data acquisition card and instantaneous power was calculated in real-time using the LabVIEW platform. The efficiency curves under the normal dual-bus mode and the fault-tolerant single-bus mode are compared in Figure 21. Under normal operation with balanced bus power, the maximum efficiency reaches 97.54%. The efficiency decreases by 2% under full and light load conditions. Under fault-tolerant single-bus mode, the maximum efficiency reaches 97.33% and decreases by 2% depending on the load condition. The loss of the FT-MAB is broken down into the normal mode and fault-tolerant mode, corresponding to the experimental efficiency curves, as shown in Figure 22.

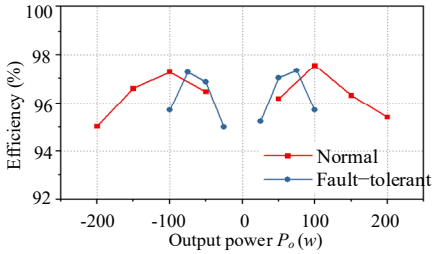

Figure 21. Experimental efficiency of the prototype.

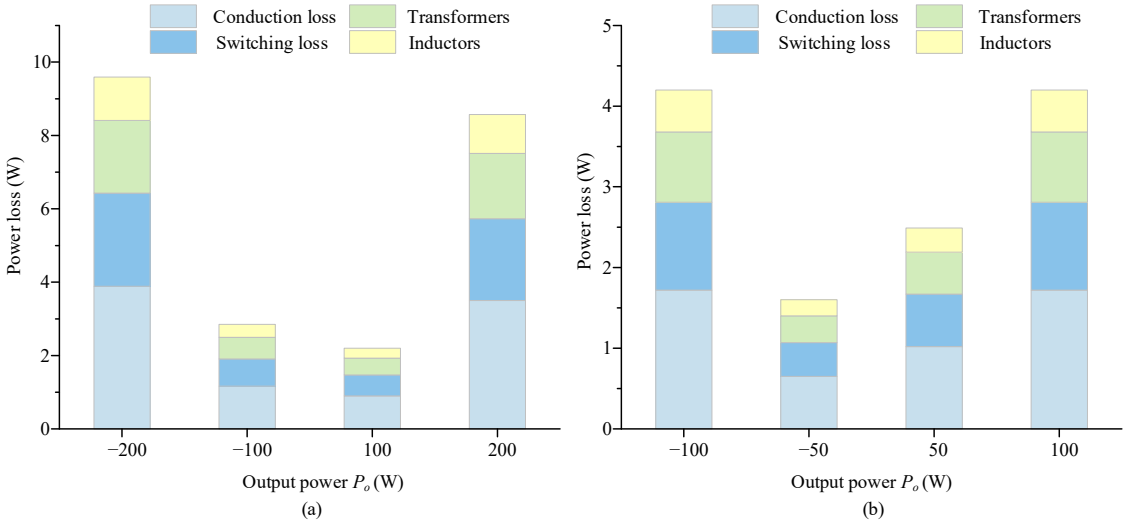

Figure 22. Power loss of the FT-MAB converter in experiments: (**a**) Normal mode and (**b**) fault-tolerant mode.

6. Conclusions

In the conventional zonal DC shipboard configuration, two sets of energy storage and power converters are required. As an alternative, a fault-tolerant multiport active bridge converter is proposed for reduced cost and power loss. The key findings of this paper are as follows:

- The proposed FT-MAB converter enables bidirectional power regulation between the energy storage and the two DC buses, as well as mutual power support between the DC buses;
- In the event of a short-circuit fault, the FT-MAB converter can isolate the fault port and maintain uninterrupted power supply to the healthy bus;
- Compared to the traditional dual-converter zonal configuration, the proposed topology can maintain fault-tolerant operation and reduce the converter power loss as well as cost.

The proposed FT-MAB topology and modulation method are tested during normal operation and short-circuit fault condition, in verification of the resilient power supply aim for zonal DC systems. The FT-MAB converter achieves flexible energy interaction among multiple buses in a shipboard zone DC system through its multi-port shared energy storage design. By continuously supplying power to healthy buses through the energy storage unit, it significantly enhances the system's power supply resilience, providing an innovative solution for high-reliability shipboard power systems.

Author Contributions: Conceptualization, J.M.; Methodology, J.M.; Software, J.M. and Y.Q.; Validation, Y.Q.; Formal analysis, J.M.; Investigation, J.M. and X.S.; Data curation, Y.C.; Writing—original draft, J.M. and Y.C.; Visualization, X.S. All authors have read and agreed to the published version of the manuscript.

Funding: This paper was supported by Science and Technology Project of State Grid Corporation (Grant Number: SGSHDK00DWJS2310324/Task Number 52090023002D).

Data Availability Statement: The original contributions presented in this study are included in the article. Further inquiries can be directed to the corresponding author.

Conflicts of Interest: The authors declare no conflict of interest.

References

1. *IEEE Std 1709-2018 (Revision of IEEE Std 1709-2010)*; IEEE Recommended Practice for 1 kV to 35 kV Medium-Voltage DC Power Systems on Ships. IEEE: Piscataway, NJ, USA, 2018; pp. 1–54.
2. Sulligoi, G.; Vicenzutti, A.; Menis, R. All-Electric Ship Design: From Electrical Propulsion to Integrated Electrical and Electronic Power Systems. *IEEE Trans. Transp. Electrif.* **2016**, *2*, 507–521.
3. Wen, S.; Jin, X.; Zheng, Y.; Wang, M. Probabilistic Coordination of Optimal Power Management and Voyage Scheduling for All-Electric Ships. *IEEE Trans. Transp. Electrif.* **2024**, *10*, 3661–3669.
4. Xu, L.; Guerrero, J.M.; Lashab, A.; Wei, B.; Bazmohammadi, N.; Vasquez, J.C.; Abusorrah, A. A Review of DC Shipboard Microgrids—Part I: Power Architectures, Energy Storage, and Power Converters. *IEEE Trans. Power Electron.* **2022**, *37*, 5155–5172.
5. Zohrabi, N.; Shi, J.; Abdelwahed, S. An overview of design specifications and requirements for the MVDC shipboard power system. *Int. J. Electr. Power Energy Syst.* **2019**, *104*, 680–693.
6. Jin, Z.; Sulligoi, G.; Cuzner, R.; Meng, L.; Vasquez, J.C.; Guerrero, J.M. Next-Generation Shipboard DC Power System: Introduction Smart Grid and dc Microgrid Technologies into Maritime Electrical Netowrks. *IEEE Electrif. Mag.* **2016**, *4*, 45–57.
7. Latorre, A.; Soeiro, T.B.; Geertsma, R.; Coraddu, A.; Polinder, H. Shipboard DC Systems—A Critical Overview: Challenges in Primary Distribution, Power-Electronics-Based Protection, and Power Scalability. *IEEE Open. J. Ind. Elec.* **2023**, *4*, 259–286.
8. Sulligoi, G.; Bosich, D.; Vicenzutti, A.; Khersonsky, Y. Design of Zonal Electrical Distribution Systems for Ships and Oil Platforms: Control Systems and Protections. *IEEE Trans. Ind. Appl.* **2020**, *56*, 5656–5669.
9. Baran, M.E.; Mahajan, N. System reconfiguration on shipboard DC zonal electrical system. In Proceedings of the IEEE Electric Ship Technologies Symposium, Philadelphia, PA, USA, 27 July 2005; pp. 86–92.
10. Maqsood, A.; Corzine, K.A. Integration of Z-Source Breakers Into Zonal DC Ship Power System Microgrids. *IEEE J. Emerg. Sel. Top. Power Electron.* **2017**, *5*, 269–277.
11. Hou, N.; Li, Y.W. Overview and Comparison of Modulation and Control Strategies for a Nonresonant Single-Phase Dual-Active-Bridge DC–DC Converter. *IEEE Trans. Power Electron.* **2020**, *35*, 3148–3172.
12. Shi, H.; Sun, K.; Wu, H.; Li, Y. A Unified State-Space Modeling Method for a Phase-Shift Controlled Bidirectional Dual-Active Half-Bridge Converter. *IEEE Trans. Power Electron.* **2020**, *35*, 3254–3265.
13. Jung, J.-H.; Kim, H.-S.; Ryu, M.-H.; Baek, J.-W. Design Methodology of Bidirectional CLLC Resonant Converter for High-Frequency Isolation of DC Distribution Systems. *IEEE Trans. Power Electron.* **2013**, *28*, 1741–1755. [CrossRef]
14. Kang, X.; Li, S.; Smedley, K.M. Decoupled PWM Plus Phase-Shift Control for a Dual-Half-Bridge Bidirectional DC–DC Converter. *IEEE Trans. Power Electron.* **2018**, *33*, 7203–7213.
15. Jakka, V.N.S.R.; Shukla, A.; Demetriades, G.D. Dual-Transformer-Based Asymmetrical Triple-Port Active Bridge (DT-ATAB) Isolated DC–DC Converter. *IEEE Trans. Ind. Electron.* **2017**, *64*, 4549–4560. [CrossRef]
16. Chen, Y.; Ma, J.; Zhu, M.; Liu, J. Dual-Mode Wide-Voltage-Range Operation of Hybrid Triple Active Bridge Converter for Bipolar DC Distribution Systems. *IEEE Trans. Ind. Appl.* **2024**, *60*, 8998–9014. [CrossRef]
17. Wang, Z.; Luo, Q.; Wei, Y.; Mou, D.; Lu, X.; Sun, P. Topology Analysis and Review of Three-Port DC–DC Converters. *IEEE Trans. Power Electron.* **2020**, *35*, 11783–11800. [CrossRef]
18. Zhang, H.; Dong, D.; Liu, W.; Ren, H.; Zheng, F. Systematic Synthesis of Multiple-Input and Multiple-Output DC–DC Converters for Nonisolated Applications. *IEEE J. Emerg. Sel. Top. Power Electron.* **2022**, *10*, 6470–6481. [CrossRef]
19. Sato, Y.; Uno, M.; Nagata, H. Nonisolated Multiport Converters Based on Integration of PWM Converter and Phase-Shift-Switched Capacitor Converter. *IEEE Trans. Power Electron.* **2020**, *35*, 455–470. [CrossRef]
20. Tao, H. Integration of Sustainable Energy Sources Through Power Electronic Converters in Small Distributed Electricity Generation Systems. Ph.D. Dissertation, Electrical Engineering, Technische Universiteit Eindhoven, Eindhoven, The Netherlands, 2008.
21. Ma, J.; Zhu, M.; Li, Y.; Cai, X. Monopolar Fault Reconfiguration of Bipolar Half Bridge Converter for Reliable Load Supply in DC Distribution System. *IEEE Trans. Power Electron.* **2022**, *37*, 11305–11318. [CrossRef]

22. Yang, W.; Ma, J.; Zhu, M.; Hu, C. Open-Circuit Fault Diagnosis and Tolerant Method of Multiport Triple Active-Bridge DC-DC Converter. *IEEE Trans. Ind. Appl.* **2023**, *59*, 5473–5487. [CrossRef]
23. Zhang, H.; Yu, H.; Zhang, Q.; Wang, Y.; Chen, Z. Fault Current Suppression for the Fault Ride-Through of Triple-Active-Bridge Converters. *IEEE Trans. Ind. Electron.* **2024**, *71*, 10727–10738. [CrossRef]
24. Xiao, Z.; Zeng, Y.; Tang, Y. Swift and Seamless Start-Up of DAB Converters in Constant and Variable Frequency Modes. *IEEE Trans. Ind. Electron.* **2024**. [CrossRef]
25. Zeng, Y.; Xiao, Z.; Liu, Q. Physics-Informed Deep Transfer Reinforcement Learning Method for the Input-Series Output-Parallel Dual Active Bridge-Based Auxiliary Power Modules in Electrical Aircraft. *IEEE Trans. Transp. Electrif.* **2024**. [CrossRef]
26. *IEEE Std 1826-2020 (Revision of IEEE Std 1826-2012)*; IEEE Standard for Power Electronics Open System Interfaces in Zonal Electrical Distribution Systems Rated Above 100 kW. IEEE: Piscataway, NJ, USA, 2020; pp. 1–44. [CrossRef]
27. Satpathi, K.; Ukil, A.; Pou, J. Short-circuit fault management in DC electric ship propulsion system: Protection requirements review of existing technologies and future research trends IEEE Trans. *IEEE Trans. Transp. Electrif.* **2018**, *4*, 272–291.
28. Digikey Electronics. 2024. Available online: https://www.digikey.cn/zh (accessed on 15 October 2024).
29. Magnetics-Inductor Design Tool. 2024. Available online: https://designtools.mag-inc.com/inductor/ (accessed on 28 October 2024).

Disclaimer/Publisher's Note: The statements, opinions and data contained in all publications are solely those of the individual author(s) and contributor(s) and not of MDPI and/or the editor(s). MDPI and/or the editor(s) disclaim responsibility for any injury to people or property resulting from any ideas, methods, instructions or products referred to in the content.